PAPER

Two-dimensional graphitic metal carbides: structure, stability and electronic properties

To cite this article: Kah-Meng Yam *et al* 2023 *Nanotechnology* **34** 465706

IOP Publishing Nanotechnology
Nanotechnology 34 (2023) 465706 (11pp) https://doi.org/10.1088/1361-6528/acedb6

Two-dimensional graphitic metal carbides: structure, stability and electronic properties

Kah-Meng Yam[1,2,5], Yongjie Zhang[1,3,5], Na Guo[4,5], Zhuoling Jiang[1], Hui Deng[3,*] and Chun Zhang[1,2,*]

[1] Department of Physics, National University of Singapore, 2 Science Drive 3 117551, Singapore
[2] Department of Chemistry, National University of Singapore, 3 Science Drive 3 117543, Singapore
[3] Department of Mechanical and Energy Engineering, Southern University of Science and Technology, Shenzhen, 518055, Guangdong, People's Republic of China
[4] NUS (Chongqing) Research Institute, No. 16 South Huashan Road, 401123, Chongqing, People's Republic of China

E-mail: dengh@sustech.edu.cn and phyzc@nus.edu.sg

Received 14 May 2023, revised 31 July 2023
Accepted for publication 7 August 2023
Published 31 August 2023

Abstract

Via first-principles computational modeling and calculations, we propose a new class of two-dimensional (2D) atomically thin crystals that contain metal-C_3 (MC_3) moieties periodically distributed in a graphenic lattice, which we refer to as 2D graphitic metal carbides (g-MCs). Most g-MCs are dynamically stable as verified by the calculated phonon spectra. Our detailed chemical bonding analyzes reveal that the high stability of g-MCs can be attributed to a unique bonding feature, which manifests as the carbon-backbone-mediated metal–metal interactions. These analyzes provide new insights for understanding the stability of 2D materials. It is found that the calculated electronic band gaps and magnetic moments (per unit cell) of g-MCs can range from 0 to 1.30 eV and 0 to 4.40 μ_B, respectively. Highly tunable electronic properties imply great potential of 2D g-MCs in various applications. As an example, we show that 2D g-MnC can be an excellent electrocatalyst towards CO_2 reductive reaction for the formation of formic acid with an exceptionally high loading of Mn atoms (~43 wt%). We expect this work to simulate new experiments for fabrication and applications of g-MCs.

Supplementary material for this article is available online

Keywords: 2D materials, graphitic metal carbides, g-MCs, chemical bonding, metal-carbon interaction

(Some figures may appear in colour only in the online journal)

1. Introduction

The realm of two-dimensional (2D) materials is burgeoning, spearheaded by graphene since its inception in 2004 [1]. Considerable effort has been devoted to the discovery of many other 2D materials [2–5], especially to overcome the shortcomings of graphene in various applications such as the lack of a sizeable electronic bandgap and the extreme chemical inertness. In the past few years, a lot of experimental and theoretical studies have demonstrated that monolayer 2D materials and 2D layered structures show extensive potential prospects in the fields of catalysis [6, 7], spintronics [8, 9], thermoelectrics [10–12], and optoelectronics [13, 14]. Among them, the combination of chemically active metal atoms and inert graphene has attracted great attention in recent years under the context of single-atom catalysis (SAC) [15–21]. Relatively weak metal-carbon interaction (compared with metal–metal interaction) results in the poor stability of metal atoms on graphene plane [15, 17, 18]. Hence, nitrogen [19, 20] and oxygen [21] anchor atoms that interact strongly with both carbon and metal atoms are often required to

[5] These authors contributed equally to this work.
[*] Authors to whom any correspondence should be addressed.

stabilize these metal atoms, but the introduction of anchor atoms would greatly disturb the 2D crystal structure, causing the material highly disordered. Another issue is that the anchor atoms may limit the metal loading rate of the system. Under the context of SAC, high metal loading rate is highly desired. Thus, to propose stable 2D metal–carbon crystals without the anchor atoms that have tunable bandgaps and chemical activities is of great interest to both fundamental study and real applications.

In this study, by extensive first principles modeling and calculations, we predict a new class of atomically thin 2D metal–carbon crystals, which are stable without the need of anchor atoms. These materials all contain metal-C_3 (MC_3) moieties periodically distributed in a graphenic lattice with M_2C_{12} (M = metal atom) being the chemical formula of the primitive cell. We therefore name these materials 2D graphitic metal carbides (g-MCs). Our chemical bonding analyzes indicate that the manifestation of the peculiar crystal structure in g-MCs as carbon-backbone-mediated metal–metal interactions can stabilize the metal atoms embedded in the carbon skeleton. Significantly, electronic structures and magnetic properties of g-MCs are highly tunable. The calculated energy band gaps (E_g) and magnetic moments per unit cell (M_{ag}) of g-MCs range from 0 to 1.30 eV and 0 to 4.40 μ_B, respectively, suggesting the great potential of g-MCs in various applications. As an example, we show that with an exceptionally high Mn loading of 43 weight percent (wt%), the predicted 2D g-MnC can facilely electrochemically synthesize formic acid (HCOOH) from carbon dioxide (CO_2) with a very modest limiting potential of only −0.42 V.

2. Computational details

All the first-principles calculations were conducted under the ground-state spin-polarized density functional theory (DFT) formalism by using the Vienna *ab initio* simulation package (VASP) [22, 23]. In all calculations, projector augmented wave pseudopotentials [24] and a plane wave basis set with a kinetic cut off energy of 500 eV were used. The generalized gradient approximation to the exchange-correlation functional was employed, in which the Perdew–Burke–Ernzerhof format was adopted [25].

For the lattice optimizations of 2D g-MCs, no symmetry constraints were imposed. The Brillouin zone was sampled by a 4 × 4 × 1 Γ-centered *k*-point grid in the Monkhorst–Pack scheme [26], and the convergence criteria were that the total energy and the residual Hellmann–Feynman force acting on each atom should be less than 10^{-4} eV and 10^{-2} eV Å^{-1}, respectively. In all 2D g-MCs models, the spurious interaction between the replicas of periodic images was eliminated by the inclusion of a vacuum space of at least 15 Å in the direction perpendicular to the atomic plane.

The cohesive energies (E_{coh}) for all ground-state g-MCs were calculated, according to the following definition, $E_{coh} = \frac{E_{g-MC} - 2E_M - 12E_C}{14}$, where E_{g-MC} denotes the total energy of one unit cell of g-MC monolayer, E_M and E_C represent the energy of an isolated metal atom and a single carbon atom in vacuum, respectively, and the denominator '14' means the total number of atoms in the unit cell. Negative values of E_{coh} indicate that it is more stable for the atoms to exist as the g-MCs instead of individual atoms. The spin-polarized *ab initio* molecular dynamics (AIMD) simulation of 2D g-MnC was performed in the canonical ensemble (NVT) with the Nosé–Hoover thermostat, where a 2 × 2 × 1 supercell of g-MnC was used. The time step was set to 1.5 fs for the simulation with a total duration of 12 ps. To verify the thermal stability of 2D g-MnC, the AIMD simulation was performed at 800 K, where the corresponding Mn_2C_{12} structure with *P*-3 space group was utilized as the original structure. The phonon band dispersions of g-MCs were obtained using the density functional perturbation theory (DFPT) implemented in VASP and phonopy, in order to verify their dynamic stabilities. In all phonon calculations, at least the corresponding 2 × 2 × 1 supercells were adopted, and each was sampled with a 4 × 4 × 1 Γ-centered *k*-mesh.

Periodic natural bonding orbital method (PNBO) [27] and its extension, the solid-state adaptive natural density partition (SSAdNDP) [28] scheme, were adopted to analyze the chemical bonding features in all ground-state g-MCs by projecting the delocalized plane wave output from the VASP code to a localized atomic basis set. The ANO-DK3 basis set was used in the projection for most of 2D g-MCs except for g-BiC and g-PdC, where the Jorge-ADZP basis set was adopted [29].

The crystal overlap Hamilton population (COHP) was conducted with the local-orbital basis suite towards electronic structure reconstruction by LOBSTER package [30, 31], which is interfaced with VASP. For all elements, the pbeVaspFit2015 basis set [32] was employed in the projections and the projections yielded charge spilling values less than 5% in all cases.

For the modeling of the electrocatalytic carbon dioxide reduction reaction (CO_2RR), a 2 × 2 × 1 supercell of g-MnC was employed. The Brillouin zone was sampled by a 3 × 3 × 1 Γ-centered *k*-point grid in the Monkhorst–Pack scheme [26] for structural optimizations and by a 5 × 5 × 1 grid for electronic structure calculations. The convergence criteria were that the total energy and the residual Hellmann–Feynman force acting on each atom should be less than 10^{-4} eV and 10^{-2} eV Å^{-1}, respectively. The adsorption energy for CO_2, E_{ads}, is defined as $E_{ads} = E_{CO_2^*} - E_{CO_2(g)} - E_*$, where $E_{CO_2^*}$, $E_{CO_2(g)}$, and E_* are the electronic energies for the adsorbed CO_2 molecule, gaseous and isolated CO_2 molecule, and g-MnC surface, respectively. The evaluation of the electrocatalytic properties was carried out under the computational hydrogen electrode (CHE) formalism [33], which allows one to make use of the following relation at any *pH* value, $\mu_{H^+} + \mu_{e^-} = \frac{1}{2}\mu_{H_2}$, and the electrochemical potential of species *A*, μ_A, was calculated as $\mu_A = G_A = E_A + E_{ZPE} - TS + eU$, where E_A is the electronic energy of species *A*, E_{ZPE} is the zero-point vibrational energy, *T* is the absolute temperature, *S* is its vibrational entropy, *e* is the fundamental charge, and *U* is the applied

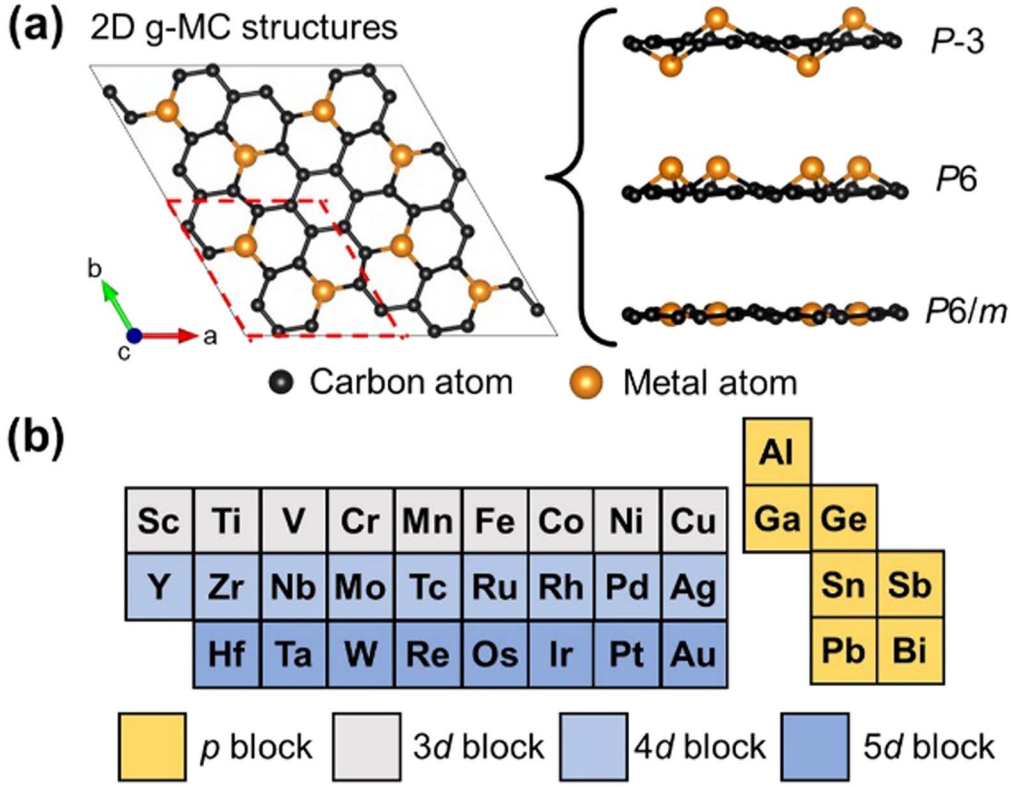

Figure 1. 2D g-MC structures. (a) Top and side views of 2D g-MC structures, showing *P*-3, *P*6, and *P*6/*m* space groups, respectively. The unit cell of 2D g-MC crystals is enclosed in red dash lines. (b) Feasible metals for forming the stable 2D g-MCs. Note that both *P*-3 and *P*6 structures are possible for these g-MCs, and *P*6/*m* structure is possible only when a large tensile strain exists.

electrode potential. Then, E_{ZPE} and S required for adsorbed species were calculated with vibrational frequencies using the harmonic approximation, and for gas-phase species using values obtained from the NIST database. The limiting potential, U_L, required to drive every elementary step exergonic is defined as $U_L = -\frac{\Delta G_{max}}{e}$, where ΔG_{max} is the most positive Gibbs free energy change between any two consecutive electrochemical steps. Based on the equilibrium potential (U_0) of CO_2RR, the overpotential (η) can then be calculated as $\eta = |U_0 - U_L|$. The visualization for electronic and structural analysis (VESTA) software [34] was used for visualization of the atomic structures and isosurfaces produced from the various codes, from which the corresponding figures are produced.

3. Results and discussion

3.1. Ground-state structures

The first instance of designing 2D carbon-based crystals involving direct bonding between carbon and metal atoms (without the use of anchor atoms) was demonstrated by Li *et al* [35], which shows that a unique 2D metal–carbon structure with the *P*-3 group symmetry in unit cell can be highly stable. In this work, we propose that 2D metal carbide crystals can have three different structures with different symmetries (as shown in figure 1(a)): *P*-3 as previously proposed, in which the metals reside on alternate plane of the carbon backbone; *P*6, in which the metal atoms are found on the same side; and *P*6/*m*, in which the carbon and metal atoms are on the same plane. As aforementioned, we name all these 2D crystals with different symmetries g-MCs. With extensive DFT based computational modeling and simulations, we explore the possibility of forming stable 2D g-MCs under these three structures with all nonradioactive metal elements in the periodic table. We have found that *s*-block metal atoms are unable to form any stable g-MCs in structure relaxation calculations; all 33 *p*- and *d*-block metal elements in the periodic table (see figure 1(b)) can produce stable g-MCs in *P*-3 structure and 31 of them (except for Pb and Ag) can also generate *P*6 structure during structure optimizations, with *P*6 being ground state for 2D g-NiC and *P*-3 being ground states for all other g-MCs. The *P*6/*m* structure is only possible for some g-MCs under large tensile strain due to the relatively large size of metal atoms, which might be interesting for some applications but will not be discussed in this work.

3.2. Stability

The calculated properties of all possible 2D g-MCs are tabulated in table 1. Prior to the discussion of electronic properties of the g-MCs, we first dwell into their stabilities, which is of paramount importance in materials design. As a preliminary check, the values of E_{coh} (see the definition in computational details) calculated for all 2D g-MCs are comparable to various stable 2D materials [35] such as g-C_3N_4,

Table 1. Tabulation of the possible structures, magnetic moment per unit cell, electronic band gaps, and dynamic stability of 2D g-MCs.

System		Possible structures	Magnetic moment (μ_B)	Band gap (eV)	Dynamically stable?
p-block	g-AlC	***P*-3**, *P*6	0	1.03	√
	g-GaC	***P*-3**, *P*6	0	0.85	√
	g-GeC	***P*-3**, *P*6	0	Metallic	√
	g-SnC	***P*-3**, *P*6	0	Metallic	√
	g-SbC	***P*-3**, *P*6	0	1.15	√
	g-PbC	***P*-3**	0	Metallic	√
	g-BiC	***P*-3**, *P*6	0	1.30	√
3*d*-block	g-ScC	***P*-3**, *P*6	0	0.51	×
	g-TiC	***P*-3,** *P*6	0	Metallic	√
	g-VC	***P*-3,** *P*6	2.44	Metallic	√
	g-CrC	***P*-3**, *P*6	4.40	Metallic	√
	g-MnC	***P*-3**, *P*6	4.00	↑: 0.29	√
	g-FeC	***P*-3,** *P*6	1.97	↑: 0.30	√
	g-CoC	***P*-3,** *P*6	0	0.19	√
	g-NiC	*P*-3, ***P*6**	0	Metallic	√
	g-CuC	***P*-3**, *P*6	0	Metallic	√
4*d*-block	g-YC	***P*-3**, *P*6	0	0.51	×
	g-ZrC	***P*-3,** *P*6	0	Metallic	√
	g-NbC	***P*-3,** *P*6	2.00	Metallic	√
	g-MoC	***P*-3**, *P*6	0	0.16	√
	g-TcC	***P*-3**, *P*6	1.74	Metallic	√
	g-RuC	***P*-3**, *P*6	0.62	Metallic	√
	g-RhC	***P*-3**, *P*6	0	0.42	√
	g-PdC	***P*-3**, *P*6	1.21	Metallic	√
	g-AgC	***P*-3**	0	Metallic	√
5*d*-block	g-HfC	***P*-3**, *P*6	0	Metallic	√
	g-TaC	***P*-3,** *P*6	1.86	Metallic	√
	g-WC	***P*-3**, *P*6	0	0.26	√
	g-ReC	***P*-3**, *P*6	1.75	Metallic	√
	g-OsC	***P*-3**, *P*6	1.96	↑: 0.51	√
	g-IrC	***P*-3**, *P*6	0	0.47	√
	g-PtC	***P*-3**, *P*6	1.60	Metallic	√
	g-AuC	***P*-3**, *P*6	0	Metallic	√

Notes: bold in black denotes the ground-state configuration. Electronic band gaps are given for semiconductors and the semiconducting channel of half metals. The arrow ↑ (↓) denotes the majority (minority) spin channel for spin-polarized systems, where applicable.

MoS_2, and *h*-BN, suggesting that most of these g-MCs should be stable. The E_{coh} alongside with some details of ground-state g-MC structures (lattice constant, M–C bond length, and height of metal atom away from carbon plane) are tabulated in table S1 in supporting information. As a more rigorous examination, we performed phonon calculations based on DFPT, and the results are shown in figures S1 (for *p*-block metals), S2 (for 3*d* block), S3 (for 4*d*-block), and S4 (for 5*d*-block) in supporting information. It is found that the phonon dispersion relations indicate that all the ground-state g-MCs are dynamically stable, except for g-ScC (figure S2(a)) and g-YC (figure S3(a)), yielding significant negative frequencies in phonon spectra.

As mentioned in introduction, metal–carbon interaction has been known not strong enough to stabilize metal atoms on 2D carbon plane. The origin of the dynamic stability of proposed g-MCs therefore is an interesting issue to study. To understand this, we analyze the bonding nature of these g-MCs using the SSAdNDP approach [28], which is an extension of the PNBO method [27, 36]. Compared with the PNBO method that can only be used to analyze chemical bonding in terms of one-center (1c) bonds (or lone pairs) and two-center (2c) bonds, SSAdNDP can identify multi-center delocalized bonds. Such feature can be helpful for understanding long-range correlations in crystals, which in turn provides insights to the chemical origin of the structure stability. The chemical bonding results for all ground-state g-MCs are summarized in table 2, and the typical 1c, 2c and multi-center bonds in g-FeC yielded from SSAdNDP analysis are shown in figure S5 in supporting information.

With a total of 14 atoms in a distorted honeycomb pattern per unit cell, the expected number of σ (covalent) bonds is 21. Clearly, the reason for the dynamic instability of g-ScC and g-YC may be well due to the inability of each of the metal atoms in forming the three expected covalent bonds with carbon atoms, resulting in six σ bonds fewer than the rest. In addition, we elucidated from the electron localization function plots (exemplified by g-ScC shown as figure S6 in supporting information) that Sc and Y atoms interact with the carbon atoms via electrostatic attractions. In fact, the absence of M–C

Table 2. Summary of the chemical bonding information in 2D g-MCs. Numbers in table are the number of corresponding bonds. The arrow ↑ (↓) denotes the majority (minority) spin channel for spin-polarized systems.

		Bond types								
				2c						
System		Bonds	1c	σC-C	π	C–C	π	4c	6c	8c
P block	g-AlC	27	0	21	3	0	3	0		
	g-GaC	27	0	21	3	0	3	0		
	g-GeC	28	0	21	3	0	3	1		
	g-SnC	28	0	21	3	2	1	1		
	g-SbC	29	2	21	3	0	3	0		
	g-PbC	28	0	21	3	2	1	1		
	g-BiC	29	2	21	3	0	3	0		
3*d* block	g-ScC	27	0	**15**	3	6	3	**0**		
	g-TiC	28	0	21	0	2	3	2		
	g-VC	↑30	0	21	0	6	3	0		
		↓28	0	21	0	2	3	2		
	g-CrC	↑32	4	21	0	2	3	2		
		↓28	0	21	0	0	3	4		
	g-MnC	↑33	6	21	3	0	3	0		
		↓29	0	21	0	2	3	3		
	g-FeC	↑33	6	21	3	0	3	0		
		↓31	0	21	0	6	3	1		
	g-CoC	33	6	21	3	0	3	0		
	g-NiC	34	6	21	3	0	3	1		
	g-CuC	35	6	21	3	0	3	2		
4*d* block	g-YC	27	0	**15**	3	6	3	**0**		
	g-ZrC	28	0	21	0	2	3	2		
	g-NbC	↑30	0	21	0	6	3	0		
		↓28	0	21	0	2	3	2		
	g-MoC	30	0	21	0	6	3	0		
	g-TcC	↑32	0	21	0	6	3	2		
		↓30	0	21	0	6	3	0		
	g-RuC	↑32	4	21	0	2	3	2		
		↓32	0	21	0	6	3	2		
	g-RhC	33	6	21	3	0	3	0		
	g-PdC	↑35	6	21	3	0	3	2		
		↓33	6	21	0	0	3	3		
	g-AgC	35	10	21	0	0	3	1		
5*d* block	g-HfC	28	0	21	0	2	3	2		
	g-TaC	↑30	0	21	0	6	3	0		
		↓28	0	21	0	2	3	2		
	g-WC	30	0	21	0	6	3	0		
	g-ReC	↑32	0	21	0	6	3	2		
		↓30	0	21	0	6	3	0		
	g-OsC	↑33	6	21	3	0	3	0		
		↓31	0	21	0	6	3	1		
	g-IrC	33	6	21	3	0	3	0		
	g-PtC	↑35	6	21	3	0	3	2		
		↓33	6	21	0	0	3	3		
	g-AuC	35	6	21	3	0	3	2		

σ covalent bonds is the reason why *s*-block metal atoms are unable to form any stable g-MCs as the metal atoms only weakly electrostatically interact with the carbon framework. Taking Na member as an example, the g-NaC structure would automatically change back to the 'Na + γ-graphyne' structure (Na + γ-GY) after the structure optimization at 0 K (shown as figure S7 in supporting information).

Amongst the three types of multi-center (4c, 6c, and 8c) bonds in g-MCs, the most familiar and uninteresting one would be the 6c bonds as they are also found in molecular phenyl (C_6H_5-) systems, which are also expected to be present in graphenic networks. The other two multi-center bonds warrant some attention, which are peculiar to g-MCs. We observe that the 8c extended bonds can be found for all

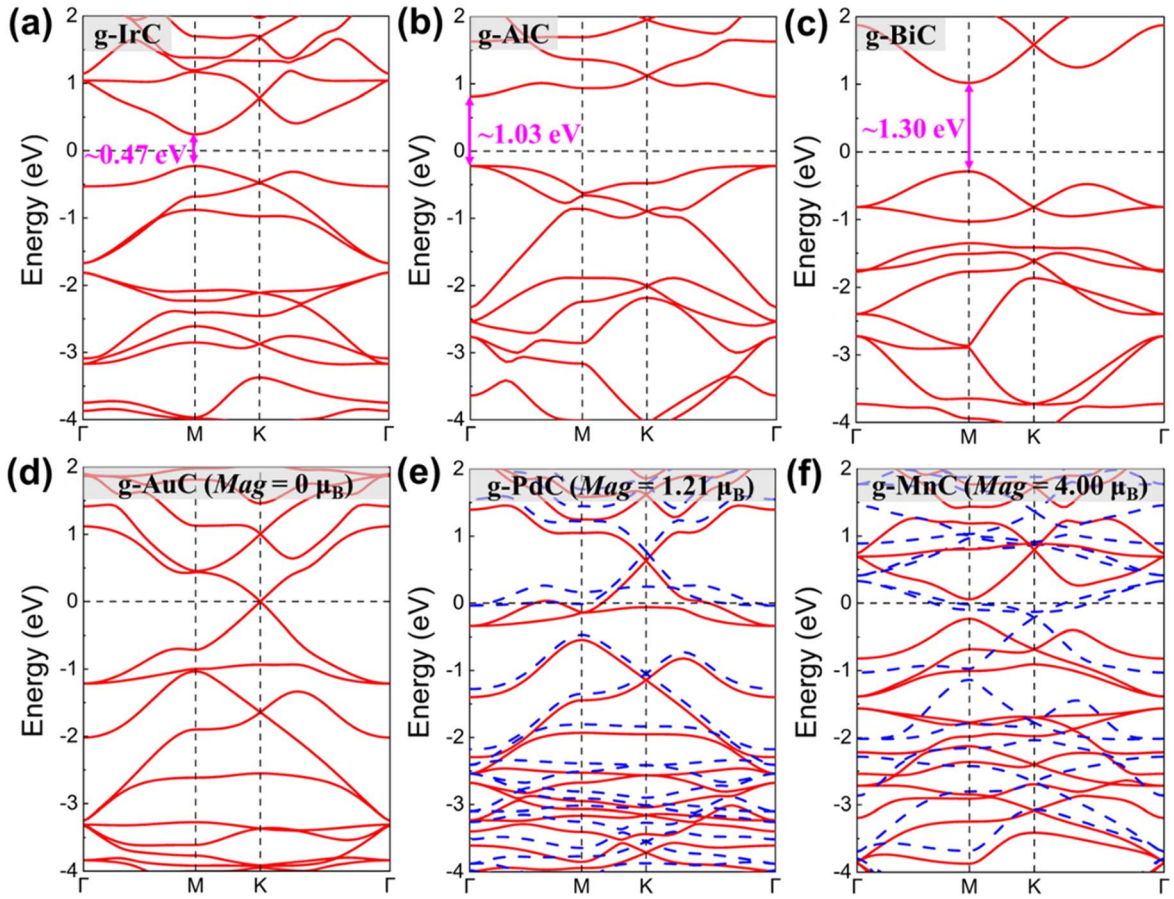

Figure 2. Band structures of some typical g-MCs. Nonmagnetic semiconductors: (a) g-IrC, (b) g-AlC, and (c) g-BiC. Metals with different magnetic moments: (d) semi-metallic g-AuC, (e) ferromagnetic g-PdC, and (f) half-metallic g-MnC. The red solid (blue dash) line represents the majority (minority) spin channel.

metallic g-MCs. Such bonds can link two metal atoms in the unit cell together via the carbon framework, as well as the 4c and the 2c σ bonds, and they suggest the existence of long-range carbon-backbone-mediated metal–metal interactions in g-MCs. It is these types of bonds that help stabilizing metal atoms in the carbon skeleton. In other words, we can say that the metal-carbon interactions and the carbon-backbone-mediated metal–metal interactions together make the materials stable. Later we will show that the long-range metal–metal interaction also plays an important role in understanding electronic properties of g-MCs.

3.3. Electronic properties

We next examine details of electronic properties, i.e. energy band gaps and magnetic moments, of g-MCs listed in table 1. As can be seen from the table, g-MCs exhibit a rich variety of electronic properties. The calculated energy band gaps and magnetic moments (per unit cell) of g-MCs range from 0 to 1.30 eV and 0 to 4.40 μ_B, respectively. Note that all *p*-block g-MCs have zero magnetic moment in one unit cell. Electronic band structures of all g-MCs calculated from spin-polarized DFT methods can be found in figures S8 (*p*-block), S9 (3*d*-block), S10 (4*d*-block), and S11 (5*d*-block) in supporting information. Electronic band structures of some typical g-MCs are shown in main text (figure 2) to demonstrate tunable properties of the family. In figures 2(a)–(c), we show band structures for nonmagnetic semiconducting g-IrC (E_g = 0.47 eV), g-AlC (E_g = 1.03 eV), and g-BiC (E_g = 1.30 eV), respectively. In figures 2(d)–(f), we show nonmagnetic semi-metal g-AuC, magnetic metal g-PdC (Mag = 1.21 μ_B), and half metal g-MnC (Mag = 4.00 μ_B), respectively. The tunable energy band gaps and magnetic moments suggest that g-MCs can be useful in various applications such as catalysis, electronics, and spintronics. It is worth mentioning here that in band structures of many *d*-block g-MCs, there exist flat bands around Fermi level (E_F). For example, there are flat bands in g-AuC (about 1.22 eV below E_F, figure 2(d)), g-PdC (about 0.34 eV below E_F, figure 2(e)), and g-MnC (about 0.69 eV above E_F, figure 2(f)). These flat bands could be useful in some applications related to strong correlated electrons [37, 38].

The magnetism in these g-MCs is of particular interest because it cannot be understood by the simple model widely used to explain the magnetism of single transition-metal (TM) atom embedded in graphene with single vacancy (TM_1@g) [16, 19, 39], despite that both TM_1@g and g-MCs contain MC_3 local bonding. The magnetism of TM_1@g can be understood by the MC_3-bonding-induced splitting of *d* orbitals of TM atoms. However, the model generates quite

different magnetic properties from those calculated for g-MCs. One striking example is that Fe_1@g is predicted to be nonmagnetic, while g-FeC is magnetic with around 1 μ_B of magnetic moment on each Fe. Similar to TM_1@g, spin densities of magnetic g-MCs are all largely localized on metal atoms. Examples of calculated spin differential densities of magnetic 3*d*-block g-MCs are shown in figure S12 in supporting information. We will show next that not only the local MC_3 bonding, but also the long-range carbon-backbone-mediated metal–metal interaction, affects the splitting of metal *d* orbitals, resulting in different magnetic properties from those of TM_1@g systems.

The analysis of magnetism shall involve energy levels corresponding to five *d*-orbitals contributed by the TM atom. Considering the MC_3 local bonding with a C_{3v} point group, five *d*-orbitals of each TM atom transform under the operations of the group to give a linear sum of the irreducible representations $A + 2E$. Out of the *d*-orbitals, d_{z^2} has '*A*' symmetry, while the other four orbitals d_{xz}, d_{yz}, d_{xy}, and $d_{x^2-y^2}$ hybridize to form two doubly degenerate pairs '*E*1' and '*E*2' in a splitting mode of '*E*1-*E*2-*A*', as shown in the band structure of Fe_1@g in figure S13 in supporting information. Note that in the case of Fe_1@g, the *d*-orbital splitting is same for both spin channels. The MC_3-induced *d*-orbital splitting shall also apply to TM atoms in g-MCs. Besides the MC_3-induced splitting, the long-range metal–metal interactions as aforementioned in g-MCs shall cause further splitting by forming bonding and anti-bonding orbitals, leading to different magnetic properties from those of TM_1@g systems.

Exemplified by g-FeC crystal, we identified 10 bands in each spin channel with significant contribution from the *d*-orbitals by calculating the projected density of states (PDOS) weighted band structure (figure 3) and by plotting the band-decomposed wavefunctions at Γ point in the first Brillouin zone (figure S14 in supporting information). The COHP curve plotted for g-FeC (figure S15 in supporting information) revealed that five, which are lower in energy, are bands resulting from bonding MC_3 states, while the rest are anti-bonding in nature [30, 31]. Note that the metal–metal interaction induced splitting is spin dependent as shown in figure S15, due to the +1 oxidation state of each Fe (suggested by Bader charge analysis). The main results of above analysis are summarized in figure 3, where we see that due to the metal–metal interaction, the MC_3-induced *E*1-*E*2-*A* states of two Fe atoms in g-FeC form five bonding orbitals and five anti-bonding orbitals (orbital with *) in the pattern of *E*1-*A*-*E*2-*E*2*-*A**-*E*1*, as shown in the PDOS weighted band structures (figure 3(a) for majority spin and figure 3(b) for minority spin). The MC_3 bonding and metal–metal interaction induced splitting of 10 *d* orbitals of two Fe atoms in one unit cell in g-FeC for both spin channels are sketched in figure 3(c). Since two Fe atoms (with +1 oxidation state) have 14 electrons in total, the E_F is between majority-spin *E*1* and minority-spin *E*2* as shown in the figure 3(c), leading to 2 μ_B of magnetic moment for two Fe atoms in one unit cell.

3.4. Applications in electrocatalysis

The high stability and tunable electronic properties of 2D g-MCs offer new opportunities for various applications in both solid-state physics (e.g. electronics) and solid-state chemistry (e.g. solid-state catalysis). As an example, here we show that 2D g-MCs could be good electrocatalysts towards the two-electron reduction reaction of CO_2 (CO_2RR) synthesizing HCOOH. The upcycling of CO_2 are important aspects in green chemistry as it contributes to the greater effort of achieving a carbon neutral energy cycle [40–42]. It has been well-known that the adsorption of CO_2 on catalyst is the key step for CO_2RR, which is very difficult because CO_2 has large energy gap. The g-MCs we proposed have advantages because of two reasons. Firstly, the class of materials exhibits a variety of electronic structures and provides us a big enough catalog to search for high-performance catalysts. Secondly, g-MCs offer exceptionally high loading of metal atoms, which is highly desired in SAC applications. Our calculations predict that the ground-state *P*-3 g-MnC is perhaps the best candidate in the class of electrocatalysts towards CO_2RR among all g-MCs. The possible synthesis route of g-MnC is shown in figure 4(a). Herein, we start from γ-GY, and then each Mn atom is placed at each hollow site of γ-GY. Interestingly, due to the strong Mn-C interaction, a self-organizing process would occur, which would lead to the significant lattice reconstruction process of the substrate, consequently forming g-MnC. Undoubtedly, the structure stability is one crucial factor that affects the performance of catalysts. The material, *P*-3 g-MnC, has been verified to be dynamically stable as seen from the phonon spectrum (figure S2(e) in supporting information). By AIMD simulations, we further show that g-MnC can maintain its structural integrity even at temperatures as high as 800 K (figure 4(b)).

We then test the adsorption of CO_2 molecule on g-MnC firstly. A CO_2 molecule would adsorb on the Mn atom in *P*-3 g-MnC through C and O atoms, i.e. CO_2 adopts a η^2(C, O) bonding mode, with the E_{ads} of −0.73 eV (see the definition in computational details). Presented in the left panel of figure 5(a) is the adsorption configuration with the charge redistribution isosurface $\Delta\rho$ superimposed. The C–O bond was elongated to 1.28 and 1.20 Å (the nonbonding end) from 1.18 Å of gas-phase CO_2, and the originally linear CO_2 was bent with a ∠OCO of 141.8°. Bader charge analysis substantiates that the adsorbate gained a net charge of 0.50 |e|. The above results strongly indicate that CO_2 molecule is activated by g-MnC. Moreover, the adsorbate is better described as η^2(C, O) − CO_2^-, which has been recently identified experimentally as the crucial first intermediate in the selectivity of CO_2RR to HCOOH [42].

The activation should ensue from the π backdonation, which can be seen from the fact that the adsorbed CO_2 molecule lost and gained electrons simultaneously as indicated by the charge redistribution isosurface in figure 5(a). The density isosurface of electron accumulation in figure 5(a) showing the electrons gained by CO_2 exhibits close resemblance to the lowest unoccupied molecular orbital (LUMO) of the bent CO_2 as shown in the right panel of figure 5(a).

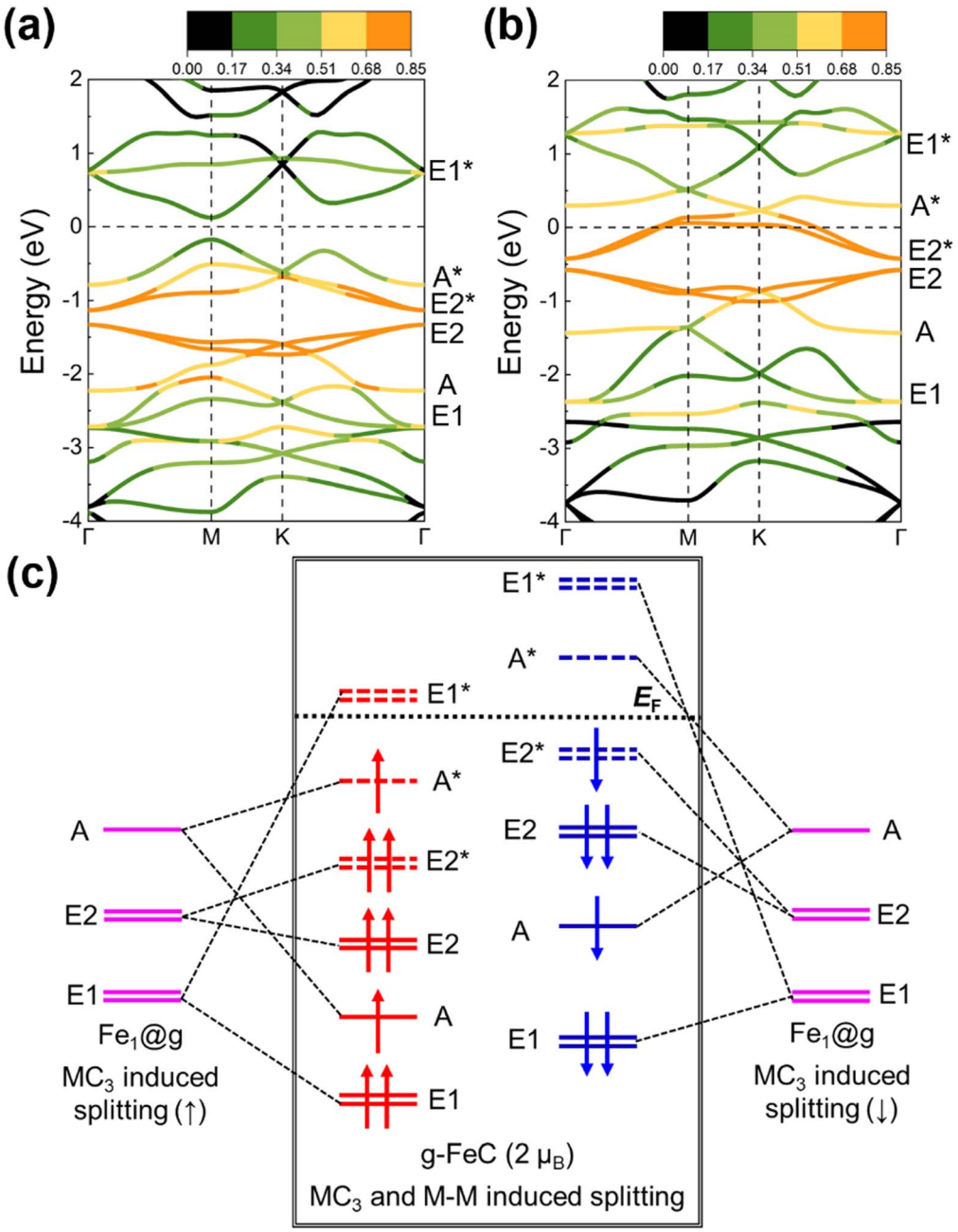

Figure 3. Magnetic states analysis for g-FeC. PDOS weighted band structures of (a) the majority and (b) the minority spin channels with the contribution from *d*-orbitals. The color bar for the band structure indicates the contribution of *d*-orbitals of Fe atoms. The 10 *d*-bands at Γ point clearly show a '*E*1-*A*-*E*2-*E*2*-*A**-*E*1*' pattern in each spin channel. (c) Energy levels for Fe$_1$@g and g-FeC. Magenta lines for Fe$_1$@g mean the split *d*-orbitals of the corresponding Fe atom. Red (blue) lines for g-FeC represent the majority (minority) spin channel of the corresponding Fe atoms. Solid (dash) lines for g-FeC denote the bonding (antibonding) states.

Therefore, the π backdonation can be rationalized as follows: the bent CO_2 is formed from the initial adsorption of linear CO_2 when electrons were transferred from CO_2 to the catalyst g-MnC (as shown by density isosurface of electron depletion around CO_2 in figure 5(a)), and then the LUMO of the bent CO_2 gain electrons from g-MnC, resulting in the overall depletion of electrons of g-MnC.

Following which, the reaction pathway for the CO_2RR forming various value-added C_1 products (i.e. HCOOH, CH_2O, CH_3OH, and CH_4) were calculated under the CHE formalism [33, 43–45]. Our results demonstrate that HCOOH can be formed facilely with an on-set potential of −0.42 V, which is the least negative amongst the various C_1 products (refer to table S2 in supporting information), and the free energy diagram for the HCOOH formation is shown in figure 5(b). Evidently, the potential determining step should be the first electrochemical hydrogenation of the adsorbed CO_2. Since the equilibrium potential of the two-electron reduction of CO_2-to-HCOOH is −0.12 V, the calculated overpotential η would be 0.30 V. Considering the intrinsic high loading of Mn atoms (∼43 wt%), 2D g-MnC could be an

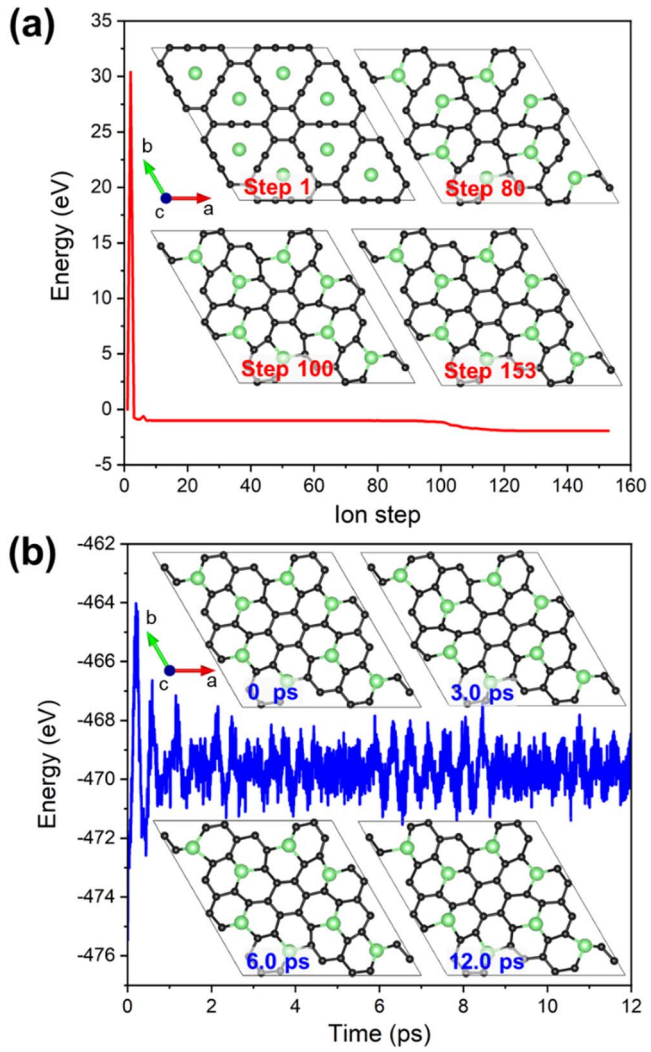

Figure 4. The formation process and thermal stability of 2D g-MnC. (a) Structure optimization of 'γ-GY + Mn' system at 0 K. The insets are the atomic configurations for the corresponding ion steps. (b) AIMD simulation of g-MnC with the *P*-3 configuration at 800 K. The insets are the corresponding snapshots of the trajectories at 0, 3.0, 6.0, and 12.0 ps, showing that the structure of 2D g-MnC remains intact after 12.0 ps of simulation. The black (green) ball represents carbon (manganese) atom.

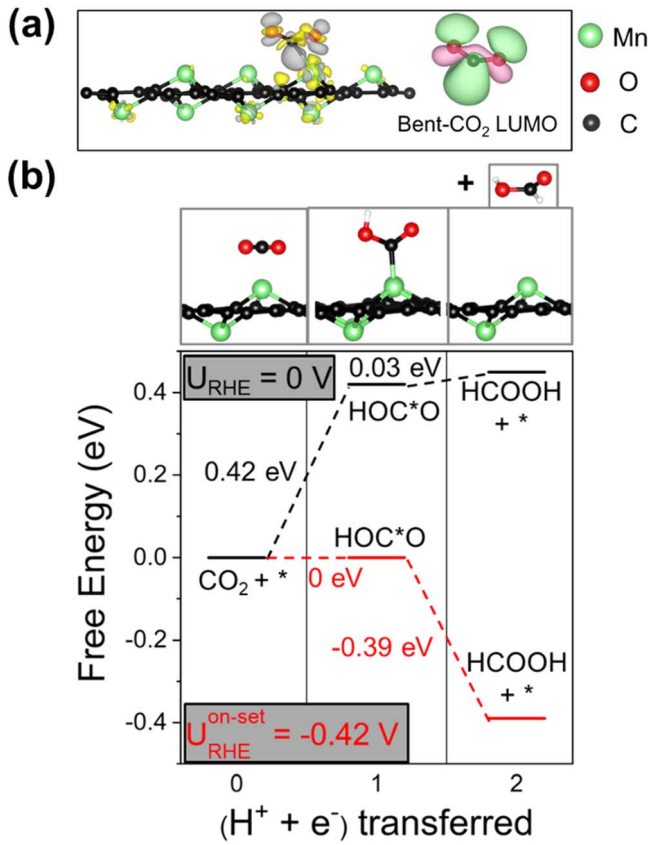

Figure 5. CO_2RR results of g-MnC. (a) Side view of CO_2 adsorption configuration on g-MnC with the isosurfaces of charge redistribution ($\Delta\rho = \rho_{CO_2@g-MnC} - \rho_{CO_2} - \rho_{g-MnC}$). Gray (yellow) represents the electron accumulation (depletion). The inset shows the LUMO of bent-CO_2. (b) Gibbs free energy diagram for the formation of HCOOH.

excellent electrocatalyst for synthesizing HCOOH via CO_2RR.

4. Conclusion

Via first-principles computational modeling and calculations, we propose a new class of atomically thin crystals, 2D graphitic metal carbides (g-MCs). These materials all contain MC_3 moieties periodically distributed in a graphenic lattice with M_2C_{12} (M = metal atom) being the chemical formula of one unit cell. Our calculations show that during structure optimizations, all 33 *p*- and *d*-block metal elements in the periodic table can produce energetically stable g-MCs in *P*-3 structure and 31 of them (with exceptions of Pb and Ag) can also generate energetically stable *P*6 structures, with *P*6 being ground state for 2D g-NiC and *P*-3 being ground states for all others. Phonon spectra for ground-state structures indicate that all g-MCs are dynamically stable, with the exceptions of g-ScC and g-YC due to their inability to form covalent bonds with carbon as revealed by the SSAdNDP analysis. The SSAdNDP analysis also suggests that the 2c, 4c, and 8c bonds present in most g-MCs can connect the two metal atoms together through the carbon backbone. The calculated energy band gaps and magnetic moments (per unit cell) of g-MCs range from 0 to 1.30 eV and 0 to 4.40 μ_B, respectively. Our detailed analysis suggests that the carbon-backbone-mediated metal–metal interactions play an important role in understanding magnetic properties of these materials. Highly tunable electronic properties imply great potential of 2D g-MCs in various applications such as 2D electronics, spintronics and catalysis. For electronics or spintronics, metallic 2D g-MCs can be considered for new types of electrodes, while tunable band gaps and magnetic moments make the semiconducting g-MCs attractive for transistors and spintronic devices. For catalysis, the high density of metal atoms on surfaces of g-MCs can be very useful. As one example, we show that 2D g-MnC could electrochemically synthesize HCOOH with a modest limiting potential (−0.42 V). Considering the exceptionally high intrinsic

loading of metal atoms of the materials, g-MCs can be promising candidates for single-atom catalyst.

These results provide a fundamental and systematic understanding of the bonding, electronic, and magnetic properties of 2D g-MCs. We expect these results to stimulate experimental work in fabricating the proposed 2D g-MCs. On a broader note, we hope that, following our work, more novel stable 2D metal-carbon-only crystals with different structures can be discovered.

Acknowledgments

CZ acknowledges the support from Ministry of Education of Singapore (MOE2019-T2-2-030) and NUS academic research fund (R-144-000-449-114). Computations were done with the NUS High Performance Computing (HPC) facilities and National Supercomputing Centre (NSCC) in Singapore.

Data availability statement

All data that support the findings of this study are included within the article (and any supplementary files).

Author contributions

CZ conceived the project. KY and YZ did calculations for geometrical and electronic structures of all materials. NG performed electrochemical computations. YZ provided the first draft. KY and CZ revised the paper. All contributed to data analysis and finalization of the paper.

Conflict of interests

The authors declare no conflict of interests.

Supporting information available

Phonon dispersion spectra of g-MCs; Bonding structures of 2D g-FeC; ELF plots of g-ScC; g-NaC and 'Na + γ-GY' structures; Band structures of ground-state g-MCs; Spin differential density plots of the magnetic g-MCs; PDOS weighted band structure of Fe_1@g; Band-decomposed wavefunctions of g-FeC; Band structure and COHP results of g-FeC; Structure and stability parameters of ground-state g-MCs; CO_2RR results with various C1 products.

ORCID iDs

Kah-Meng Yam https://orcid.org/0000-0002-8463-5358
Yongjie Zhang https://orcid.org/0009-0004-4919-5862
Chun Zhang https://orcid.org/0000-0002-1581-5806

References

[1] Novoselov K S, Geim A K, Morozov S V, Jiang D, Zhang Y, Dubonos S V, Grigorieva I V and Firsov A A 2004 Electric field effect in atomically thin carbon films *Science* **306** 666–9
[2] Pacilé D, Meyer J C, Girit Ç Ö and Zettl A 2008 The two-dimensional phase of boron nitride: few-atomic-layer sheets and suspended membranes *Appl. Phys. Lett.* **92** 133107
[3] Bhimanapati G R *et al* 2015 Recent advances in two-dimensional materials beyond graphene *ACS Nano* **9** 11509–39
[4] Yang L M, Bacic V, Popov I A, Boldyrev A I, Heine T, Frauenheim T and Ganz E 2015 Two-dimensional Cu_2Si monolayer with planar hexacoordinate copper and silicon bonding *J. Am. Chem. Soc.* **137** 2757–62
[5] Manzeli S, Ovchinnikov D, Pasquier D, Yazyev O V and Kis A 2017 2D transition metal dichalcogenides *Nat. Rev. Mater.* **2** 17033
[6] Xu H, Cheng D, Cao D and Zeng X C 2018 A universal principle for a rational design of single-atom electrocatalysts *Nat. Catal.* **1** 339–48
[7] Fei H *et al* 2018 General synthesis and definitive structural identification of MN_4C_4 single-atom catalysts with tunable electrocatalytic activities *Nat. Catal.* **1** 63–72
[8] Yam K M, Guo N and Zhang C 2018 Two-dimensional Cu_2Si sheet: a promising electrode material for nanoscale electronics *Nanotechnology* **29** 245704
[9] Feng Y P, Shen L, Yang M, Wang A, Zeng M, Wu Q, Chintalapati S and Chang C R 2017 Prospects of spintronics based on 2D materials *WIREs Comput. Mol. Sci.* **7** e1313
[10] Sun S, Shi X L, Liu W D, Wu T, Wang D, Wu H, Zhang X, Wang Y, Liu Q and Chen Z G 2022 Cheap, large-scale, and high-performance graphite-based flexible thermoelectric materials and devices with supernormal industry feasibility *ACS Appl. Mater. Interfaces* **14** 8066–75
[11] Shi X L, Liu W D, Li M, Sun Q, Xu S D, Du D, Zou J and Chen Z G 2022 A solvothermal synthetic environmental design for high-performance SnSe-based thermoelectric materials *Adv. Energy Mater.* **12** 2200670
[12] Zheng Z-H *et al* 2022 Harvesting waste heat with flexible Bi_2Te_3 thermoelectric thin film *Nat. Sustain.* **6** 180–91
[13] Tan T, Jiang X, Wang C, Yao B and Zhang H 2020 2D material optoelectronics for information functional device applications: status and challenges *Adv. Sci.* **7** 2000058
[14] Cheng Z, Cao R, Wei K, Yao Y, Liu X, Kang J, Dong J, Shi Z, Zhang H and Zhang X 2021 2D materials enabled next-generation integrated optoelectronics: from fabrication to applications *Adv. Sci.* **8** e2003834
[15] Gan Y, Sun L and Banhart F 2008 One- and two-dimensional diffusion of metal atoms in graphene *Small* **4** 587–91
[16] Lu Y-H, Zhou M, Zhang C and Feng Y-P 2009 Metal-embedded graphene: a possible catalyst with high activity *J. Phys. Chem.* C **113** 20156–60
[17] Rodríguez-Manzo J A, Cretu O and Banhart F 2010 Trapping of metal atoms in vacancies of carbon nanotubes and graphene *ACS Nano* **4** 3422–8
[18] Markevich A V, Baldoni M, Warner J H, Kirkland A I and Besley E 2016 Dynamic behavior of single Fe atoms embedded in graphene *J. Phys. Chem.* C **120** 21998–2003
[19] Yam K, Guo N, Jiang Z, Li S and Zhang C 2020 Graphene-based heterogeneous catalysis: role of graphene *Catalysts* **10** 53
[20] Yang H B *et al* 2018 Atomically dispersed Ni(i) as the active site for electrochemical CO_2 reduction *Nat. Energy* **3** 140–7
[21] Yan H *et al* 2018 Atomic engineering of high-density isolated Co atoms on graphene with proximal-atom controlled reaction selectivity *Nat. Commun.* **9** 3197

[22] Kresse G and Hafner J 1993 *Ab initio* molecular dynamics for liquid metals *Phys. Rev.* B **47** 558–61
[23] Kresse G and Furthmüller J 1996 Efficient iterative schemes for *ab initio* total-energy calculations using a plane-wave basis set *Phys. Rev.* B **54** 11169–86
[24] Blochl P E 1994 Projector augmented-wave method *Phys. Rev.* **50** 17953–79
[25] Perdew J P, Burke K and Ernzerhof M 1996 Generalized gradient approximation made simple *Phys. Rev. Lett.* **77** 3865–8
[26] Monkhorst H J and Pack J D 1976 Special points for Brillouin-zone integrations *Phys. Rev.* B **13** 5188–92
[27] Dunnington B D and Schmidt J R 2012 Generalization of natural bond orbital analysis to periodic systems: applications to solids and surfaces via plane-wave density functional theory *J. Chem. Theory Comput.* **8** 1902–11
[28] Galeev T R, Dunnington B D, Schmidt J R and Boldyrev A I 2013 Solid state adaptive natural density partitioning: a tool for deciphering multi-center bonding in periodic systems *Phys. Chem. Chem. Phys.* **15** 5022–9
[29] Pritchard B P, Altarawy D, Didier B, Gibson T D and Windus T L 2019 New basis set exchange: an open, up-to-date resource for the molecular sciences community *J. Chem. Inf. Model.* **59** 4814–20
[30] Dronskowski R and Blöchl P E 1993 Crystal orbital hamilton populations (COHP). Energy-resolved visualization of chemical bonding in solids based on density-functional calculations *J. Phys. Chem.* **97** 8617–24
[31] Maintz S, Deringer V L, Tchougreeff A L and Dronskowski R 2013 Analytic projection from plane-wave and PAW wavefunctions and application to chemical-bonding analysis in solids *J. Comput. Chem.* **34** 2557–67
[32] Maintz S, Deringer V L, Tchougreeff A L and Dronskowski R 2016 LOBSTER: a tool to extract chemical bonding from plane-wave based DFT *J. Comput. Chem.* **37** 1030–5
[33] Nørskov J K, Rossmeisl J, Logadottir A, Lindqvist L, Kitchin J R, Bligaard T and Jónsson H 2004 Origin of the overpotential for oxygen reduction at a fuel-cell cathode *J. Phys. Chem.* B **108** 17886–92
[34] Momma K and Izumi F 2011 VESTA 3 for three-dimensional visualization of crystal, volumetric and morphology data *J. Appl. Cryst.* **44** 1272–6
[35] Li S, Yam K-M, Guo N, Zhao Y and Zhang C 2021 Highly stable two-dimensional metal-carbon monolayer with interpenetrating honeycomb structures *NPJ 2D Mater. Appl.* **5** 52
[36] Glendening E D, Landis C R and Weinhold F 2011 Natural bond orbital methods *WIREs Comput. Mol. Sci.* **2** 1–42
[37] Yin J-X *et al* 2019 Negative flat band magnetism in a spin–orbit-coupled correlated kagome magnet *Nat. Phys.* **15** 443–8
[38] You J Y, Gu B, Su G and Feng Y P 2022 Emergent kagome electrides *J. Am. Chem. Soc.* **144** 5527–34
[39] Krasheninnikov A V, Lehtinen P O, Foster A S, Pyykko P and Nieminen R M 2009 Embedding transition-metal atoms in graphene: structure, bonding, and magnetism *Phys. Rev. Lett.* **102** 126807
[40] Sreejyothi P and Mandal S K 2020 From CO_2 activation to catalytic reduction: a metal-free approach *Chem. Sci.* **11** 10571–93
[41] Park J, Cho M, Rhee Y M and Jung Y 2021 Theoretical study on the degree of CO_2 activation in CO_2-coordinated Ni(0) complexes *ACS Omega* **6** 7646–54
[42] Chernyshova I V, Somasundaran P and Ponnurangam S 2018 On the origin of the elusive first intermediate of CO_2 electroreduction *Proc. Natl. Acad. Sci. USA* **115** E9261–70
[43] Nie X, Luo W, Janik M J and Asthagiri A 2014 Reaction mechanisms of CO_2 electrochemical reduction on Cu(111) determined with density functional theory *J. Catal.* **312** 108–22
[44] Feng J, Gao H, Zheng L, Chen Z, Zeng S, Jiang C, Dong H, Liu L, Zhang S and Zhang X 2020 A Mn-N_3 single-atom catalyst embedded in graphitic carbon nitride for efficient CO_2 electroreduction *Nat. Commun.* **11** 4341
[45] Fu L, Wang R, Zhao C, Huo J, He C, Kim K-H and Zhang W 2021 Construction of Cr-embedded graphyne electrocatalyst for highly selective reduction of CO_2 to CH_4: a DFT study *Chem. Eng. J.* **414** 128857